

Nonlinear response of silicon photonic crystal microresonators excited via an integrated waveguide and fiber taper

Paul E. Barclay, Kartik Srinivasan, and Oskar Painter

Department of Applied Physics, California Institute of Technology, Pasadena, CA 91125, USA.
phone: (626) 395-6269, fax: (626) 795-7258

pbarclay@caltech.edu

Abstract: A technique is demonstrated which efficiently transfers light between a tapered standard single-mode optical fiber and a high-Q, ultra-small mode volume, silicon photonic crystal resonant cavity. Cavity mode quality factors of 4.7×10^4 are measured, and a total fiber-to-cavity coupling efficiency of 44% is demonstrated. Using this efficient cavity input and output channel, the steady-state nonlinear absorption and dispersion of the photonic crystal cavity is studied. Optical bistability is observed for fiber input powers as low as $250 \mu\text{W}$, corresponding to a dropped power of $100 \mu\text{W}$ and 3 fJ of stored cavity energy. A high-density effective free-carrier lifetime for these silicon photonic crystal resonators of ~ 0.5 ns is also estimated from power dependent loss and dispersion measurements.

© 2005 Optical Society of America

OCIS codes: (060.1810) Couplers, switches, and multiplexers; (130.3120) Integrated optics devices; (190.1450) Bistability; (190.4390) Nonlinear optics, integrated optics

References and links

1. K. Srinivasan, P. Barclay, O. Painter, J. Chen, A. X. Cho, and C. Gmachl, "Experimental demonstration of a high quality factor photonic crystal microcavity," *Appl. Phys. Lett.* **83**, 1915–1917 (2003).
2. Y. Akahane, T. Asano, B.-S. Song, and S. Noda, "High-Q photonic nanocavity in a two-dimensional photonic crystal," *Nature* **425**, 944–947 (2003).
3. K. Srinivasan, P. E. Barclay, M. Borselli, and O. Painter, "Optical-fiber based measurement of an ultra-small volume high-Q photonic crystal microcavity," *Phys. Rev. B* **70**, 081306(R) (2004).
4. B. Lev, K. Srinivasan, P. E. Barclay, O. Painter, and H. Mabuchi, "Feasibility of detecting single atoms using photonic bandgap cavities," *Nanotechnology* **15**, S556–S561 (2004).
5. T. Yoshie, A. Scherer, J. Hendrickson, G. Khitrova, H. Gibbs, G. Rupper, C. Ell, O. Shchekin, and D. Deppe, "Vacuum Rabi splitting with a single quantum dot in a photonic crystal nanocavity," *Nature* **432**, 200–203 (2004).
6. J. Reithmaier, G. Sek, A. Löffler, C. Hofmann, S. Kuhn, S. Reitzenstein, L. Keldysh, V. Kulakovskii, and T. Reinecke, "Strong coupling in a single quantum dot-semiconductor microcavity system," *Nature* **432**, 197–200 (2004).
7. E. Peter, P. Senellart, D. Martrou, A. Lemaitre, and J. Bloch, "Exciton photon strong-coupling regime for a single quantum dot in a microcavity," <http://arxiv.org/quant-ph/0411076> (2004).
8. A. R. Cowan and J. F. Young, "Optical bistability involving photonic crystal microcavities and Fano line shapes," *Phys. Rev. E* **68**, 046606 (2003).
9. M. Soljačić, S. G. Johnson, Y. Fink, and J. D. Joannopoulos, "Optimal bistable switching in nonlinear photonic crystals," *Phys. Rev. E* **66**, 055601 (2002).
10. J.-M. Gerard, "Solid-state cavity-quantum electrodynamics with self-assembled quantum dots" in *Single Quantum Dots: Fundamentals, Applications, and New Concepts*, P. Michler ed. (Springer-Verlag, Germany, 2003), 269–314.

11. G. Brassard, N. Lutkenhaus, T. Mor, and B. Sanders, "Limitations on practical quantum cryptography," *Phys. Rev. Lett.* **85**, 1330–1333 (2000).
12. E. Knill, R. Laflamme, and G. Millburn, "A scheme for efficient quantum computation with linear optics," *Nature* **409**, 46–52 (2001).
13. A. Kiraz, M. Atatüre, and A. Imamoglu, "Quantum-dot single-photon sources: Prospects for applications in linear optics quantum optics processing," *Phys. Rev. A* **69**, 032305 (2004).
14. M. F. Yanik, S. Fan, and M. Soljačić, "High-contrast all-optical bistable switching in photonic crystal microcavities," *Appl. Phys. Lett.* **83**, 2739–2781 (2003).
15. M. Pelton, C. Santori, J. Vuckovic, B. Zhang, G. Solomon, J. Plant, and Y. Yamamoto, "An Efficient Source of Single Photons: A Single Quantum Dot in a Micropost Microcavity," *Phys. Rev. Lett.* **89**, 299602 (2002).
16. J. McKeever, A. Boca, A. D. Boozer, R. Miller, J. R. Buck, A. Kuzmich, and H. J. Kimble, "Deterministic Generation of Single Photons from One Atom Trapped in a Cavity," *Science* **303**, 1992–1994 (2004).
17. S. J. McNab, N. Moll, and Y. A. Vlasov, "Ultra-low loss photonic integrated circuit with membrane-type photonic crystal waveguides," *Opt. Express* **11**, 2927–2939 (2003), <http://www.opticsexpress.org/abstract.cfm?URI=OPEX-11-22-2927>.
18. M. Notomi, A. Shinya, S. Mitsugi, and H.-Y. Ryu, "Waveguides, resonators and their coupled elements in photonic crystal slabs," *Opt. Express* **12**, 1551–1561 (2004), <http://www.opticsexpress.org/abstract.cfm?URI=OPEX-12-8-1551>.
19. W. Bogaerts, D. Taillaert, B. Luysaert, P. Dumon, J. V. Campenhout, P. Bienstman, R. Baets, V. Wiaux, and S. Beckx, "Basic structures for photonic integrated circuits in silicon-on-insulator," *Opt. Express* **12**, 1583–1591 (2004), <http://www.opticsexpress.org/abstract.cfm?URI=OPEX-12-8-1583>.
20. A. R. Cowan, G. W. Rieger, and J. F. Young, "Nonlinear transmission of 1.5 m pulses through single-mode silicon-on-insulator waveguide structures," *Opt. Expr.* **12**, 1611–1621 (2004), <http://www.opticsexpress.org/abstract.cfm?URI=OPEX-12-8-1611>.
21. P. E. Barclay, K. Srinivasan, M. Borselli, and O. Painter, "Efficient input and output optical fiber coupling to a photonic crystal waveguide," *Opt. Lett.* **29**, 697–699 (2004).
22. M. Lončar, D. Nedeljković, T. Doll, J. Vučković, A. Scherer, and T. P. Pearsall, "Waveguiding in planar photonic crystals," *Appl. Phys. Lett.* **77**, 1937–1939 (2000).
23. J. Knight, G. Cheung, F. Jacques, and T. Birks, "Phase-matched excitation of whispering-gallery-mode resonances by a fiber taper," *Opt. Lett.* **22**, 1129–1131 (1997).
24. P. E. Barclay, K. Srinivasan, and O. Painter, "Design of photonic crystal waveguides for evanescent coupling to optical fiber tapers and integration with high-Q cavities," *J. Opt. Soc. Am. B* **20**, 2274–2284 (2003).
25. K. Srinivasan and O. Painter, "Momentum Space Design of High-Q Photonic Crystal Nanocavities in Two-Dimensional Slab Waveguides," *Opt. Express* **10**, 670–684 (2002), <http://www.opticsexpress.org/abstract.cfm?URI=OPEX-10-15-670>.
26. S. M. Spillane, T. J. Kippenberg, O. J. Painter, and K. J. Vahala, "Ideality in a Fiber-Taper-Coupled Microresonator System for Application to Cavity Quantum Electrodynamics," *Phys. Rev. Lett.* **91**, 043902 (2003).
27. S. Y. Lin, E. Chow, S. G. Johnson, and J. D. Joannopoulos, "Direct measurement of the quality factor in a two-dimensional photonic crystal microcavity," *Opt. Lett.* **26**, 1903–1905 (2001).
28. M. Dinu, F. Quochi, and H. Garcia, "Third-order nonlinearities in silicon at telecom wavelengths," *Appl. Phys. Lett.* **82**, 2954–2956 (2003).
29. T. Liang and H. Tsang, "Role of free carriers from two photon absorption in Raman amplification in silicon-on-insulator waveguides," *Appl. Phys. Lett.* **84**, 2745–2757 (2004).
30. K. Kanamoto, S. Lan, N. Ikeda, Y. Tanaka, Y. Sugimoto, K. Asakawa, and H. Ishikawa, "Single Photonic-Crystal Defect Switch for All-Optical Ultrafast Operation Using Two Photon Absorption," *IEICE Trans. Electron.* **E87-C**, 1142–1146 (2004).
31. H. W. Tan, H. M. van Driel, S. L. Schweizer, R. B. Wehrspohn, and U. Gösele, "Nonlinear optical tuning of a two-dimensional silicon photonic crystal," *Phys. Rev. B* **70**, 205110 (2004).
32. G. P. Agrawal and N. K. Dutta, *Semiconductor Lasers* (Van Nostrand Reinhold, New York, NY, 1993).
33. S. G. Johnson, M. Ibanescu, M. A. Skorobogatiy, O. Weisberg, J. D. Joannopoulos, and Y. Fink, "Perturbation theory for Maxwell's equations with shifting material boundaries," *Phys. Rev. E* **65**, 066611 (2002).
34. R. A. Soref and B. R. Bennett, "Electrooptical Effects in Silicon," *IEEE J. Quan. Elec.* **23**, 123–129 (1987).
35. In using this approximate theory, in which regions of high two-photon absorbed power are correlated with high steady-state carrier density, we better approximate the cavity "volume" of interest, and consequently the effective free-carrier lifetime better represents the average time a free-carrier stays in the region of the PC cavity mode.
36. V. R. Almeida, C. A. Barrios, R. R. Panepucci, and M. Lipson, "All-optical control of light on a silicon chip," *Nature* **431**, 1081–1084 (2004).
37. V. R. Almeida and M. Lipson, "Optical bistability on a silicon chip," *Opt. Lett.* **29**, 2387–2389 (2004).
38. T. Carmon, L. Yang, and K. J. Vahala, "Dynamical thermal behavior and thermal self-stability of microcavities," *Opt. Express* **12**, 4742–4750 (2004), <http://www.opticsexpress.org/abstract.cfm?URI=OPEX-12-20-4742>.
39. R. W. Boyd, *Nonlinear Optics*, 2nd ed. (Academic Press, San Diego, CA, 2003).
40. R. Claps, V. Raghunathan, D. Dimitropoulos, and B. Jalali, "Influence of nonlinear absorp-

- tion on Raman amplification in Silicon waveguides,” *Opt. Express* **12**, 2774–2780 (2004), <http://www.opticsexpress.org/abstract.cfm?URI=OPEX-12-12-2774>.
41. H. Rong, A. Liu, R. Nicolaescu, M. Paniccia, O. Cohen, and D. Hak, “Raman gain and nonlinear optical absorption measurements in a low-loss silicon waveguide,” *Appl. Phys. Lett.* **85**, 2196–2198 (2004).
 42. P. E. Barclay, K. Srinivasan, M. Borselli, and O. Painter, “Probing the dispersive and spatial properties of planar photonic crystal waveguide modes via highly efficient coupling from optical fiber tapers,” *Appl. Phys. Lett.* **85**, 4–6 (2004).
 43. H. M. Gibbs, *Optical bistability: controlling light with light* (Academic Press, Orlando, FL, 1985).
 44. Note that the sharp transition edge associated with optical bistability occurs at the cavity resonance wavelength when scanning from blue to red.
 45. M. Borselli, K. Srinivasan, P. E. Barclay, and O. Painter, “Rayleigh scattering, mode coupling, and optical loss in silicon microdisks,” *Appl. Phys. Lett.* **85**, 3693–3695 (2004).
 46. P.-T. Lee, J. R. Cao, S.-J. Choi, Z.-J. Wei, J. O’Brien, and P. D. Dapkus, “Operation of photonic crystal membrane lasers above room temperature,” *Appl. Phys. Lett.* **81**, 3311–3313 (2002).
 47. A. Cutolo, M. Iodice, P. Spirito, and L. Zeni, “Silicon Electro-Optic Modulator Based on a Three Terminal Device Integrated in a Low-Loss Single-Mode SOI Waveguide,” *J. Lightwave Technol.* **15**, 505–518 (1997).
 48. G. Cocorullo and I. Rendina, “Thermo-optical modulation at 1.5 μm in silicon etalon,” *IEE Electron Lett.* **28**, 83–85 (1992).
-

1. Introduction

Recently it has been demonstrated that resonant microcavities formed in planar photonic crystals (PC) are capable of not only confining light to ultra-small optical mode volumes, but also of realizing photon cavity lifetimes large enough [1, 2, 3] to enable, for instance, reaching strong-coupling with atomic Cs [4] or semiconductor quantum dots [5, 6, 7]. The enhancement to the local energy density enabled by PC cavities is also of significant interest in nonlinear optics, as it reduces the input power required for nonlinear effects, such as optical bistability [8, 9]. However, in addition to requiring large field enhancements and photon lifetimes, many of the proposed applications of PC cavities in quantum, nonlinear, and integrated optics demand the ability to efficiently interface the PC cavity with external optics. For example, using high-Q PC cavities for chip based cavity-QED (cQED) [4] or in single-photon sources [10], where photon collection is an important measure of device performance [11, 12, 13], requires an efficient coupling scheme to the sub-micron cavity mode. Similarly, proposed applications of microresonators in nonlinear-optical switching circuits [14] put a premium on reduced input power and efficient optical coupling techniques.

The difficulty in optically accessing PC cavities is largely a result of their ultra-small mode volume and external radiation pattern, which unlike micropost [15] and Fabry-Pérot [16] cavities, is not inherently suited to coupling with conventional free-space or fiber optics. Only recently have low-loss fiber coupling techniques to planar photonic crystal waveguides been demonstrated experimentally, using on-chip spot size converters ($\sim 1\text{-}4$ dB loss/port [17, 18]), out-of plane diffraction gratings ($\sim 8\text{-}10$ dB loss/port [19, 20]), and narrow-band evanescent coupling (~ 0.1 dB loss/port [21]). In this paper we employ the latter technique to efficiently source and collect light from a silicon (Si) high-Q PC cavity via a photonic crystal waveguide (PCWG) [22] which is evanescently coupled to a fiber taper [23]. Using a mode-matched PCWG-PC cavity design [24] to minimize parasitic loading of the PC cavity, cavities loaded to 60% of critical and maintaining a Q -factor close to 4×10^4 are demonstrated, and a total fiber-to-cavity coupling efficiency of 44% is measured. The utility of this efficient fiber coupling technique is then demonstrated in studies of the power dependent nonlinear response of the PC cavity. We observe optical bistability for 100 μW dropped cavity power, and predict sub-nanosecond free carrier lifetimes in the cavity.

An outline of the paper is as follows. We begin in Section 2 with a description of the fiber-to-cavity coupling scheme, with specific emphasis on issues associated with the complex modal properties of a photonic crystal microcavity. In Section 3 we augment this linear theory

by incorporating nonlinear processes which depend upon the magnitude of the internally stored cavity energy. Low power measurements of a fabricated silicon photonic crystal waveguide-cavity system are presented in Section 4, where optical fiber taper probing is used to both confirm the localized nature of a PC cavity resonance and to study the losses in the fiber-cavity system. Higher power measurements in which nonlinear effects become apparent are studied in Section 5, and the model presented in Section 3 is used to estimate the scale of the different nonlinear processes within the silicon PC cavity. Finally, a summary is given in Section 6.

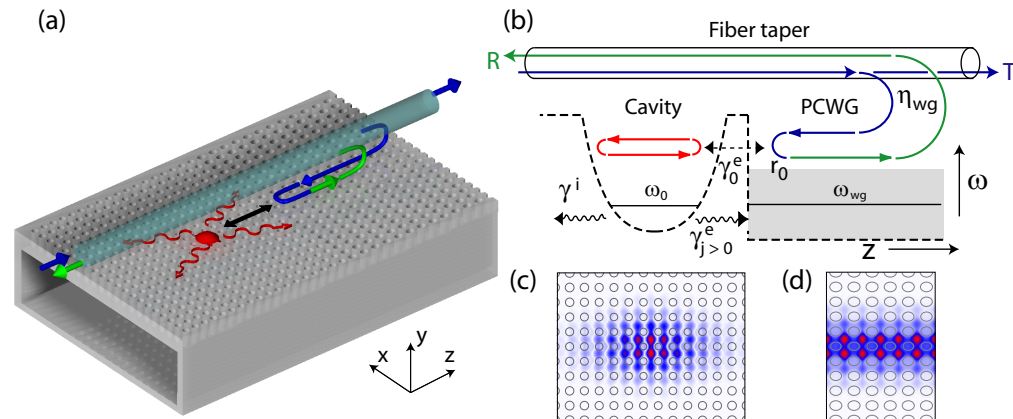


Fig. 1. (a) Schematic of the fiber taper to PC cavity coupling scheme. The blue arrow represents the input light, some of which is coupled contradirectionally into the PCWG. The green arrow represents the light reflected by the PC cavity and recoupled in the backwards propagating fiber mode. The red colored region represents the cavity mode and its radiation pattern. (b) Illustration of the fiber-PC cavity coupling process. The dashed line represents the “local” band-edge frequency of the photonic crystal along the waveguide axis. The step discontinuity in the bandedge at the PCWG - PC cavity interface is due to a jump in the longitudinal (\hat{z}) lattice constant (see Fig. 2). The parabolic “potential” is a result of the longitudinal grade in hole radius of the PC cavity. The bandwidth of the waveguide is represented by the gray shaded area. Coupling between the cavity mode of interest (frequency ω_0) and the mode matched PCWG mode ($\omega_{WG} = \omega_0$) is represented by γ_0^e , coupling to radiating PCWG modes is represented by $\gamma_{j>0}^e$, and intrinsic cavity loss is represented by γ^i . (c,d) Magnetic field profile, calculated using FDTD, of the high-Q PC cavity A_2^0 mode and the fundamental TE_1 PCWG mode, respectively.

2. Coupling scheme - theory

An illustration of the coupling scheme is shown in Figs. 1(a) and 1(b). In this scheme, evanescent coupling between an optical fiber taper and a PCWG is used to interface with the PC chip. Once on the chip, light is guided to a PC microcavity at the terminus of the PCWG. Light that is reflected from the PC cavity is then recoupled into the backward propagating fiber taper mode, where it is separated from the forward propagating input signal using a fiber splitter. In this way a single optical fiber is used to both source and collect light from the PC microcavity.

The PC waveguide and PC microcavity studied here are formed from a two-dimensional photonic crystal consisting of a square lattice array of air holes in an optically thin slab waveguide. This PC cavity-waveguide system was previously studied theoretically in Ref. [24], where the fundamental (TE_1) mode of the PCWG was designed to mode-match with the high-Q fundamental (A_2^0) cavity mode [25]. The mode pattern of the TE_1 PCWG mode and the A_2^0 cavity

mode, calculated using the finite-difference time-domain (FDTD) method, are shown in Fig. 1(c) and Fig. 1(d), respectively. The mode-matched cavity acts as a mirror with high modal reflectivity, $r_o(\omega)$, except at frequencies of the localized cavity states, where light can resonantly tunnel between the PCWG and the cavity. Previous studies have shown that the optical fiber-PCWG evanescent coupler has near unity coupling efficiency (97%) over a bandwidth of roughly 15 nm [21], thus providing the necessary efficient fiber-chip optical interface. Also, in an independent study, the fundamental A_2^0 mode of the graded square lattice PC cavity was measured to have a Q -factor of 4×10^4 and a mode localization consistent with an effective mode volume of $V_{\text{eff}} = 0.9(\lambda/n)^3$ [3].

Here we combine these two complementary components, and study the efficiency with which the PC cavity is loaded by the mode-matched, fiber-coupled PCWG. We begin with a review of some of the key parameters describing the loading of a general resonant structure, pointing out specific implications for planar PC microcavities.

2.1. Efficient waveguide to cavity loading

As proposed in Ref. [26] in the context of microsphere resonators, the interaction between a PC cavity and an external PC waveguide can be described by two key parameters, the *coupling parameter* K and the *ideality factor* I :

$$K \equiv \frac{\gamma_0^e}{\gamma^i + \sum_{j \neq 0} \gamma_j^e}, \quad (1)$$

$$I \equiv \frac{\gamma_0^e}{\sum_j \gamma_j^e}, \quad (2)$$

where the cavity mode is characterized by its resonance frequency (ω_o), its intrinsic photon loss rate in absence of the external PCWG (γ^i), and its coupling rates to the fundamental TE_1 mode (γ_0^e) and higher order (including radiating) modes of the external PCWG ($\gamma_{j>0}^e$). I describes the degree of “good” loading, via the PCWG TE_1 mode in this case, relative to the total loading of the resonator. K is the ratio of “good” loading to the parasitic and intrinsic loss channels of the resonator.

The on-resonance fraction of optical power reflected by the cavity back into the PCWG mode is determined by the coupling parameter K ,

$$R_o(\omega_o) = \frac{(1-K)^2}{(1+K)^2}. \quad (3)$$

The remaining fractional power, $1 - R_o(\omega_o)$, is absorbed inside the PC cavity or radiated into the parasitic output channels. The reflection resonance full-width at half-maximum (FWHM) linewidth is given by the sum of the loss rates for *all* of the loss channels of the cavity, $\delta\omega = \gamma^i + \sum_j \gamma_j^e$. From $R_o(\omega_o)$ and $\delta\omega$ the quality factor of the PC cavity mode due to intrinsic and parasitic loss (i.e., those loss channels other than the “good” PCWG TE_1 channel) can be determined,

$$Q_{i+P} = 2Q_T \frac{1}{1 \pm \sqrt{R_o(\omega_o)}} = Q_T(1+K), \quad (4)$$

where the total loaded quality factor is $Q_T = \omega_o/\delta\omega$, and where the \pm corresponds to the under- and over-coupled ($K \leq 1$) loading condition. On resonance, full power transfer (critical coupling) from the “good” loading channel to the resonant PC cavity mode occurs when $K = 1$.

Whereas K determines the amount of power dropped by the resonator, the role of I is more subtle. In the case of an internal emitter, the collection efficiency (η_0) of emitted photons into

the “good” loading channel is given by,

$$\eta_0 = \frac{\gamma_0^e}{\gamma^i + \sum_j \gamma_j^e} = \frac{1}{1 + 1/K}. \quad (5)$$

which depends only upon the coupling parameter K . However, the cost of obtaining a large collection efficiency is measured by the drop in loaded quality factor of the resonant cavity mode, which can be written in terms of K , I , and Q_i as

$$\frac{Q_T}{Q_i} = 1 - \frac{K}{(I(1+K))} = 1 - \frac{\eta_0}{I}. \quad (6)$$

Thus, for a given collection efficiency, to maintain a long cavity photon lifetime, I should be maximized.

Utilizing a cavity loading method with $I \sim 1$ is also important for cavity based nonlinear optics. A simple argument can be made by studying the stored energy inside a resonant cavity for a given input power. One can write for the on-resonance internal stored energy U ,

$$U = (1 - R_o(\omega_o)) \frac{Q_{i+P}}{\omega_o} P_i = \frac{4K}{(1+K)^2} \frac{I - K(1-I)}{I} \frac{Q_i}{\omega_o} P_i \quad (7)$$

where P_i is the input power in the “good” loading channel. The maximum stored energy in the resonator occurs at $K_{\max} = I/(2 - I)$, giving a peak stored energy $U_{\max} = I(Q_i/\omega_o)P_i$, which scales directly with I .

The integrated PC cavity-waveguide design employed here has two important features which serve to maximize I : (i) the waveguide and cavity modes have similar transverse field profiles (see Figs. 1(c-d)) which allows the cavity to be efficiently loaded end-on, and (ii) the end-fire PCWG-cavity geometry restricts the cavity to a single dominant output channel, in contrast to side-coupled [2], in-line [27], and direct taper coupled [3] geometries, in which the cavity radiates equally into backward and forward propagating waveguide modes (bounding $K \leq 1$ and $I \leq 0.5$). In comparison to other microcavity systems, the geometry of the PC cavity-waveguide studied here is analogous to a Fabry-Pérot cavity with a high reflectivity back mirror and a lower reflectivity front mirror through which a mode-matched input beam sources the cavity. The geometry is also similar to a side-coupled traveling wave resonator, such as a microsphere or microdisk that supports whispering-gallery type modes, in which the traveling wave resonance radiates selectively into a single phase matched output channel.

3. Influence of nonlinear absorption and dispersion on cavity response - theory

Owing to the ultra-small mode volume and long resonant photon lifetimes of the PC cavities studied here, the resulting stored electromagnetic energy density can be extremely large even for modest input powers ($< \text{mW}$), resulting in highly nonlinear behavior of the resonant cavity system. In order to account for nonlinear effects one may modify the (linear) analysis of Section 2.1 by allowing the various cavity and coupling parameters to depend upon the stored cavity energy, a reasonably easy quantity to estimate from experimental measurements. In this section, relevant nonlinear processes are explicitly incorporated into the description of the cavity response through use of carefully defined effective modal volumes and confinement factors appropriate to nonlinear processes in high-index contrast photonic crystal structures. We begin with a description of nonlinear absorption, which tends to drive the steady-state nonlinear response of the PC cavities studied here.

3.1. Nonlinear absorption

Nonlinear absorption adds power dependent loss channels to the photonic crystal cavity, degrading the quality factor as the internal cavity energy is increased, which in turn modifies the coupling efficiency from the PCWG loading channel. This effect is incorporated into the formalism presented in Section 2.1 by writing the intrinsic cavity loss rate, γ^i , explicitly in terms of its various linear and nonlinear components:

$$\gamma^i(U) = \gamma_{\text{rad}} + \gamma_{\text{lin}} + \bar{\gamma}_{\text{TPA}}(U) + \bar{\gamma}_{\text{FCA}}(U). \quad (8)$$

At low power, the ‘‘cold cavity’’ loss rate is given by γ_{rad} and γ_{lin} , which represent loss due to radiation and linear material absorption, respectively. Power dependent nonlinear loss is given here by $\bar{\gamma}_{\text{TPA}}$ and $\bar{\gamma}_{\text{FCA}}$, which represent two-photon and free-carrier absorption, respectively; other nonlinear absorption processes can be included analogously. The coupling parameter K and the quality factor Q_{i+P} depend on γ^i , requiring the solution of a system of self-consistent equations for U in order to determine the on-resonance cavity response for a given PCWG input power P_i :

$$U = \frac{4K(U)}{(1+K(U))^2} \frac{Q_{i+P}(U)}{\omega_o} P_i, \quad (9)$$

$$K(U) = \frac{\gamma_o^e}{\gamma^i(U) + \sum_{j>0} \gamma_j^e}, \quad (10)$$

$$\frac{\omega_o}{Q_{i+P}(U)} = \gamma^i(U) + \sum_{j>0} \gamma_j^e. \quad (11)$$

Before Eqs. (9 - 11) can be solved, explicit expressions for the energy-dependent contributions to γ^i are required. Beginning with relations for nonlinear absorption in bulk media, and taking into account the complicated geometry of the PC cavity, we now derive expressions for $\bar{\gamma}_{\text{TPA}}$ and $\bar{\gamma}_{\text{FCA}}$. These expressions can be written in terms of the internal cavity energy, known material parameters, and modal parameters which account for the mode shape and localization of the PC cavity field.

3.1.1. Two-photon absorption

The 1500 nm operating band of the devices studied in this work lies in the bandgap of the host silicon material. For the doping densities of the p-type silicon membrane used to form the PC cavity ($\rho \sim 1 - 3 \Omega \cdot \text{cm}$, $N_A < 10^{16} \text{ cm}^{-3}$), free-carrier absorption due to ionized dopants is small ($\alpha_{fc} \sim 10^{-2} \text{ cm}^{-1}$). Two-photon absorption however, is significant[20, 28, 29, 30, 31], especially in the highly localized PC cavities. For a given field distribution, the (time-averaged) two-photon absorption loss rate at position \mathbf{r} can be written as

$$\gamma_{\text{TPA}}(\mathbf{r}) = \beta'(\mathbf{r}) \frac{1}{2} \epsilon_o n^2(\mathbf{r}) E^2(\mathbf{r}), \quad (12)$$

where $E(\mathbf{r})$ is the *amplitude* of the complex electric field pattern $\mathbf{E}(\mathbf{r})$ of the resonant mode of the cavity, ϵ_o is the permittivity of free space, and $n(\mathbf{r})$ is the local (unperturbed) refractive index. The real, physical electric field of the resonant cavity mode can be written in terms of the complex mode pattern as $\mathbf{E}(\mathbf{r}, t) = (\mathbf{E}(\mathbf{r})e^{-i\omega_o t} + \mathbf{E}^*(\mathbf{r})e^{+i\omega_o t})/2$. The *material* parameter, β' , describes the strength of the two-photon absorption process, and can be related to the usual two-photon absorption coefficient, β , which relates intensity to loss per unit length, by $\beta' = (c/n_g)^2 \beta$, where c is the speed of light in vacuum and n_g is the group velocity index associated with the measurement of β . Typically, for bulk material measurements where waveguiding is minimal and material dispersion is small, n_g can be taken to be equal to n .

In high-index-contrast photonic crystals, E , n , and β' depend strongly on spatial coordinate \mathbf{r} . Equation (12) describes the local two-photon absorption rate; the effective modal two-photon absorption rate which characterizes the absorption of the entire cavity mode is given by a weighted average of the local absorption rate [32, 33]

$$\bar{\gamma}_{\text{TPA}} = \frac{\int \gamma_{\text{TPA}}(\mathbf{r}) n^2(\mathbf{r}) E^2(\mathbf{r}) d\mathbf{r}}{\int n^2(\mathbf{r}) E^2(\mathbf{r}) d\mathbf{r}} = \bar{\beta}' \frac{U}{V_{\text{TPA}}}, \quad (13)$$

where $\bar{\beta}'$ and V_{TPA} are defined as,

$$\bar{\beta}' = \frac{\int \beta'(\mathbf{r}) n^4(\mathbf{r}) E^4(\mathbf{r}) d\mathbf{r}}{\int n^4(\mathbf{r}) E^4(\mathbf{r}) d\mathbf{r}} \quad (14)$$

$$V_{\text{TPA}} = \frac{(\int n^2(\mathbf{r}) E^2(\mathbf{r}) d\mathbf{r})^2}{\int n^4(\mathbf{r}) E^4(\mathbf{r}) d\mathbf{r}}. \quad (15)$$

In a photonic crystal formed by air holes in silicon, $\beta'(\mathbf{r}) = \beta'_{\text{Si}}$ inside the silicon and $\beta'(\mathbf{r}) = 0$ in the air, so that Eq. (13) can be written as,

$$\bar{\gamma}_{\text{TPA}} = \Gamma_{\text{TPA}} \beta'_{\text{Si}} \frac{U}{V_{\text{TPA}}} \quad (16)$$

$$\Gamma_{\text{TPA}} = \frac{\int_{\text{Si}} n^4(\mathbf{r}) E^4(\mathbf{r}) d\mathbf{r}}{\int n^4(\mathbf{r}) E^4(\mathbf{r}) d\mathbf{r}}, \quad (17)$$

for which \int_{Si} only integrates over the silicon region of the PC cavity.

3.1.2. Free-carrier absorption

Although, as mentioned above, the (linear) free-carrier absorption due to the ionized dopants of the silicon layer used for the PC cavities in this work is negligible on the scale of other losses, two-photon absorption gives rise to a steady-state population of electron and hole free-carriers far above this equilibrium value. Two-photon absorption induced free-carrier absorption thus plays a significant role in the silicon PC cavity nonlinear response. At position \mathbf{r} in the cavity, assuming a simple Drude model, the optical loss rate due to free-carrier absorption is

$$\gamma_{\text{FCA}} = \sigma'(\mathbf{r}) N(\mathbf{r}), \quad (18)$$

where σ' is related to the material dependent free-carrier cross-section, σ , by $\sigma' = \sigma(c/n_g)$, and $N(\mathbf{r})$ is the free-carrier density. In silicon it has been demonstrated experimentally [34] that this model correctly describes absorption by both electrons and holes, albeit with unique values of $\sigma'_{e,h}$ for each carrier type. Here we let N represent the number of electron-hole pairs and take $\sigma' = \sigma'_e + \sigma'_h$. We neglect the small ($< 1 \times 10^{16} \text{ cm}^{-3}$) background free-carrier hole density due to the ionized acceptors of the p-type Si layer used in this work.

In general, the derivation of the free-carrier density for a given two-photon absorbed power distribution requires a microscopic theory taking into account carrier diffusion, carrier-carrier scattering effects (Auger recombination for instance), and in the highly porous PC cavities, local surface recombination effects. In lieu of such an analysis, we approximate the free-carrier density distribution by considering the local two-photon absorbed power,

$$N(\mathbf{r}) = \frac{\tau p_{\text{TPA}}(\mathbf{r})}{2\hbar\omega_o}, \quad (19)$$

where τ is a free-carrier lifetime, and $p_{\text{TPA}}(\mathbf{r})$ is the local absorbed power *density* due to two-photon absorption,

$$p_{\text{TPA}}(\mathbf{r}) = \frac{1}{2} \epsilon_0 n^2(\mathbf{r}) E^2(\mathbf{r}) \gamma_{\text{TPA}}(\mathbf{r}). \quad (20)$$

Equation (19) neglects non-local effects due to spatial carrier diffusion by assuming that $N(\mathbf{r})$ depends only on the power absorbed at position \mathbf{r} ; however, it does correlate regions of strong two-photon absorption with high free-carrier density. Also, since τ generally depends on N and on the proximity to surfaces, τ will have a spatial dependence within the cavity. We neglect this effect here, and let τ represent an effective free-carrier lifetime for all the carriers in the cavity region [35]. Combining Eqs. (18), (19) and (20), an effective modal free-carrier absorption rate can be written as

$$\bar{\gamma}_{\text{FCA}} = \frac{\frac{\tau}{2\hbar\omega_0} \int (\sigma'(\mathbf{r}) \frac{1}{2} \epsilon_0 n^2(\mathbf{r}) E^2(\mathbf{r}) \gamma_{\text{TPA}}(\mathbf{r})) n^2(\mathbf{r}) E^2(\mathbf{r}) d\mathbf{r}}{\int n^2(\mathbf{r}) E^2(\mathbf{r}) d\mathbf{r}}. \quad (21)$$

Substituting Eq. (12) for $\gamma_{\text{TPA}}(\mathbf{r})$, the modal loss rate due to free-carrier absorption in the porous silicon photonic crystals considered here can be written as

$$\bar{\gamma}_{\text{FCA}} = \Gamma_{\text{FCA}} \left(\frac{\tau \sigma'_{\text{Si}} \beta'_{\text{Si}}}{2\hbar\omega_0} \frac{U^2}{V_{\text{FCA}}^2} \right), \quad (22)$$

with effective confinement factor and mode volume defined as

$$\Gamma_{\text{FCA}} = \frac{\int_{\text{Si}} n^6(\mathbf{r}) E^6(\mathbf{r}) d\mathbf{r}}{\int n^6(\mathbf{r}) E^6(\mathbf{r}) d\mathbf{r}} \quad (23)$$

$$V_{\text{FCA}}^2 = \frac{(\int n^2(\mathbf{r}) E^2(\mathbf{r}) d\mathbf{r})^3}{\int n^6(\mathbf{r}) E^6(\mathbf{r}) d\mathbf{r}}. \quad (24)$$

Equations (22) and (16) represent the total loss rate of photons from the cavity due to free-carrier and two-photon absorption, respectively. These expressions depend only on material parameters, modal confinement factors $\Gamma_{\text{TPA},\text{FCA}}$, effective mode volumes $V_{\text{TPA},\text{FCA}}$, and the internal cavity energy U . The modal parameters take account of the non-trivial geometry and field distribution of the cavity mode, and can be determined for a given mode from FDTD simulations. Including expressions (16) and (22) in γ^i , Eqs. (9 - 11) can be solved iteratively for Q_{i+P} and K , which characterize the on-resonance nonlinear response of the cavity for a given input power.

3.2. Nonlinear and thermal dispersion

In addition to modifying the cavity quality factor, large cavity energy densities also modify the refractive index of the cavity, resulting in a power dependent resonance frequency. Here we consider the role of the Kerr effect, free-carrier dispersion, and heating due to linear and non-linear absorption, on the dispersive response of the PC cavity. The refractive index shift induced through the processes considered here is a function of both space and internal cavity energy. The corresponding renormalization of the resonant cavity frequency can be approximated using first order perturbation theory as

$$\frac{\Delta\omega_0(U)}{\omega_0} = -\Delta\bar{n}(U), \quad (25)$$

where the normalized modal index shift, $\Delta\bar{n}(U)$, is given by an average of the (normalized) local refractive index shift $\Delta n(\mathbf{r})/n(\mathbf{r})$,

$$\Delta\bar{n}(U) = \frac{\int (\frac{\Delta n(\mathbf{r})}{n(\mathbf{r})}) n^2(\mathbf{r}) E^2(\mathbf{r}) d\mathbf{r}}{\int n^2(\mathbf{r}) E^2(\mathbf{r}) d\mathbf{r}}. \quad (26)$$

This energy dependent frequency shift, together with the energy dependent loss described in Section 3.1, modifies the Lorentzian frequency dependence of the cavity response:

$$R_o(\omega) = 1 - \frac{4K(U)}{(1+K(U))^2} \frac{(\delta\omega/2)^2}{(\omega - \omega_o - \Delta\omega_o(U))^2 + (\delta\omega(U)/2)^2}. \quad (27)$$

For a given input power P_i and frequency ω , U is given by

$$U = \frac{P_d}{\gamma_{i+P}} = (1 - R_o(\omega)) \frac{Q_{i+P}(U)}{\omega_o} P_i, \quad (28)$$

where $P_d = (1 - R_o(\omega))P_i$ is the frequency dependent dropped power in the resonant cavity.

For input powers sufficient to shift $\Delta\omega_o > \sqrt{3}\delta\omega/2$, the frequency response described by Eq. (27) is bistable, and can be exploited for applications including temperature locking and optical switching [36, 37, 38]. In order to solve Eq. (27) for the cavity response, it is necessary to derive expressions for each of the constituents of $\Delta\bar{n}$ as a function of U . We begin with the Kerr effect.

3.2.1. Kerr effect

The time-averaged local index shift induced by the Kerr effect is

$$\Delta n_{\text{Kerr}}(\mathbf{r}) = n'_2(\mathbf{r}) \frac{1}{2} \epsilon_o n^2(\mathbf{r}) E^2(\mathbf{r}), \quad (29)$$

where $n'_2(\mathbf{r})$ is a material parameter, and is related to the usual n_2 coefficient relating intensity to refractive index shift [39] by $n'_2 = (c/n_g)n_2$. In a silicon PC cavity, neglecting the tensor nature of the third order susceptibility, the normalized modal index change due to the Kerr effect can be written as

$$\Delta\bar{n}_{\text{Kerr}}(U) = \frac{\Gamma_{\text{Kerr}}}{n_{\text{Si}}} \left(n'_{2,\text{Si}} \frac{U}{V_{\text{Kerr}}} \right), \quad (30)$$

with $n'_{2,\text{Si}}$ and n_{Si} the Kerr coefficient and linear refractive index of Si, respectively. A similar, more general expression, is given in Ref. [9]. As both the Kerr effect and two-photon absorption (TPA) share the same dependence on field strength, the confinement factor and effective mode volume associated with the Kerr effect are equal to those of TPA,

$$\Gamma_{\text{Kerr}} = \Gamma_{\text{TPA}} \quad (31)$$

$$V_{\text{Kerr}} = V_{\text{TPA}}. \quad (32)$$

3.2.2. Free-carrier dispersion

Dispersion due to free-carrier electron-hole pairs is given by¹

$$\Delta n_{\text{FCD}}(\mathbf{r}) = -\zeta(\mathbf{r})N(\mathbf{r}), \quad (34)$$

where $\zeta(\mathbf{r})$ is a material parameter with units of volume. Following the derivation of $\bar{\gamma}_{\text{FCA}}$, the normalized modal index change is

$$\Delta\bar{n}_{\text{FCD}}(U) = -\frac{\Gamma_{\text{FCD}}}{n_{\text{Si}}} \left(\frac{\tau\zeta_{\text{Si}}\beta'_{\text{Si}}}{2\hbar\omega_o} \frac{U^2}{V_{\text{FCD}}^2} \right), \quad (35)$$

¹Experimental results [34] indicate that this Drude model must be modified slightly to accurately describe the contribution from hole free-carriers in silicon, which scales with $N_h^{0.8}$:

$$\Delta n_{\text{FCD,Si}} = -[\zeta_{e,\text{Si}}N_e + (\zeta_{h,\text{Si}}N_h)^{0.8}]. \quad (33)$$

For simplicity, we ignore this in the following analysis, and note that the modification is straightforward, and is included in later numerical results.

with

$$\Gamma_{\text{FCD}} = \Gamma_{\text{FCA}} \quad (36)$$

$$V_{\text{FCD}} = V_{\text{FCA}}. \quad (37)$$

3.2.3. Thermal dispersion

It is also necessary to consider the effect of thermal heating due to optical absorption on the refractive index of the PC cavity. The normalized modal index shift is given by

$$\Delta\bar{n}_{\text{th}} = \frac{\int \left(\frac{1}{n(\mathbf{r})} \frac{dn}{dT}(\mathbf{r}) \Delta T(\mathbf{r}) \right) n^2(\mathbf{r}) E^2(\mathbf{r}) d\mathbf{r}}{\int n^2(\mathbf{r}) E^2(\mathbf{r}) d\mathbf{r}}. \quad (38)$$

Here $\Delta T(\mathbf{r})$ is the local temperature change due to the absorbed optical power density within the cavity, and dn/dT is a material dependent thermo-optical coefficient. Neglecting differences in the spatial distributions of the contributions to $\Delta T(\mathbf{r})$ from the various absorption processes, and assuming that $\Delta T(\mathbf{r})$ scales linearly with absorbed power density for a fixed spatial heating distribution, the modal thermal shift can be written as

$$\Delta\bar{n}_{\text{th}}(U) = \frac{\Gamma_{\text{th}}}{n_{\text{Si}}} \left(\frac{dn_{\text{Si}}}{dT} \frac{dT}{dP_{\text{abs}}} P_{\text{abs}}(U) \right) \quad (39)$$

where,

$$P_{\text{abs}}(U) = (\gamma_{\text{lin}} + \bar{\gamma}_{\text{TPA}}(U) + \bar{\gamma}_{\text{FCA}}(U^2)) U. \quad (40)$$

$\Gamma_{\text{th}} = \int_{\text{Si}} n^2 E^2 d\mathbf{r} / \int n^2 E^2 d\mathbf{r}$ is a confinement factor which accounts for the fact that only the semiconductor experiences an appreciable index shift, and dT/dP_{abs} is the thermal resistance of the PC cavity which relates the mean modal temperature change to the total absorbed power. In what follows we lump these two factors together, yielding an effective thermal resistance of the PC cavity.

From Eqs. (30), (35), and (39), the total modal index change and corresponding resonance frequency shift can be determined as a function of cavity energy. The nonlinear lineshape described by Eq. (27) can then be calculated iteratively as a function of input power when combined with the power dependent loss model of sub-section 3.1. This is used below in Section 5 to estimate the scale of the different nonlinear processes in silicon PC microcavities.

As a final comment we note that the above analysis has assumed a steady-state optical, carrier, and thermal distribution, whereas the transient response of such structures is of significant practical interest for applications such high as speed switching. Although the Kerr nonlinearity, two-photon absorption, free-carrier absorption, and free-carrier dispersion all depend on the electronic structure of the semiconductor material, the sub-micron geometry typical of photonic crystals can also play an important role. For example, the surfaces introduced by the slab and air hole geometry of planar PC cavities can significantly modify the free-carrier lifetime τ compared to that in bulk material [36, 40, 41]. Similarly, the thermal response time scales inversely with the spatial scale of the optically absorbing region, and depends upon the geometry and material dependent thermal properties of a given structure [39]. Although not the focus of the work presented here, an inkling of these effects is seen in the sub-nanosecond estimated effective free-carrier lifetime in the silicon PC cavity studied below.

4. Demonstration of efficient coupling into a high-Q cavity mode

The integrated PC cavity-PCWG devices described in Section 2 were fabricated in an optically thin layer (thickness 340 nm) of silicon as described in Ref. [42]. A typical device is shown in

Fig. 2, which also shows the regions in which unpatterned silicon was removed to allow taper probing of the PC devices. In addition to isolating the PC devices on a mesa of height $\sim 10 \mu\text{m}$, a trench extending diagonally from the cavity was defined. This allowed the cavity to be probed directly by the fiber taper as in Ref. [3]. Much more efficient coupling to the PC cavity was performed using the scheme described in Section 2 by aligning the fiber taper along the axis of the PCWG and coupling through the PCWG into the PC cavity. The fiber taper was mounted in a “u”-shape on a DC motor z -stage with 50 nm encoder resolution, providing accurate vertical placement of the taper above the Si chip. In the measurements described below the taper was held fixed in the x - y plane parallel to the Si chip surface, and in-plane positioning of the Si chip was performed using a pair of DC motor stages with similar encoder resolution. A rotation and goniometer stage, mounted to the x - y stages, was used to align the in-plane and vertical angle of the sample relative to the taper, respectively. The entire sample and taper system was enclosed in an acrylic box to reduce taper fluctuations due to air currents in the room. Further details of the fiber taper fabrication and mounting geometry can be found in Refs. [3, 21, 42].

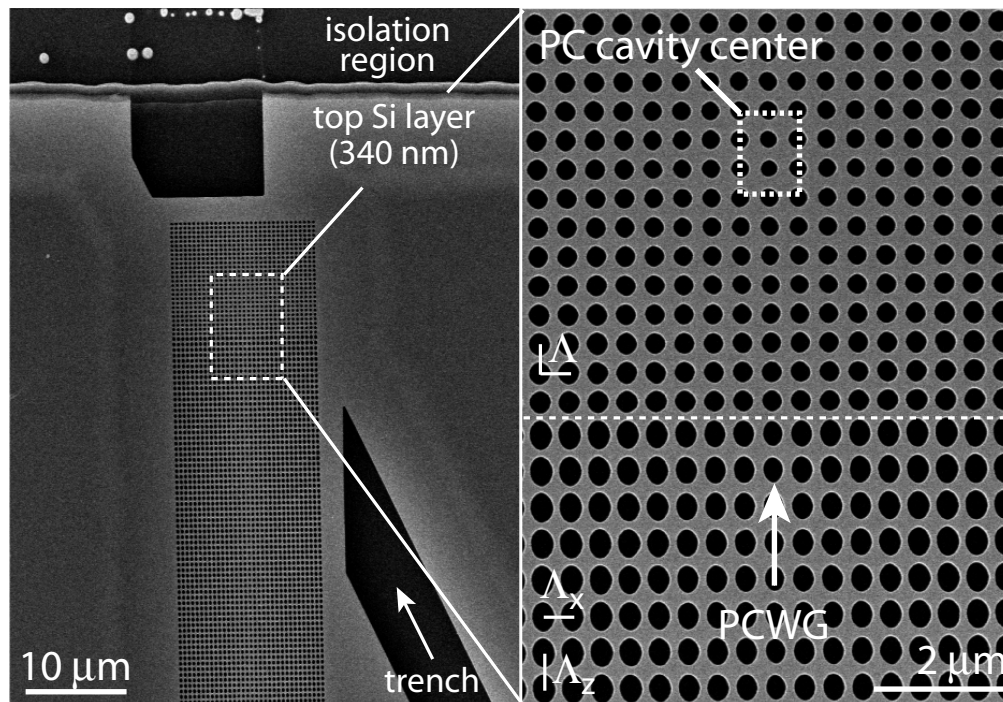


Fig. 2. SEM image of an integrated PCWG-PC cavity sample. The PC cavity and PCWG have lattice constants $\Lambda \sim 430 \text{ nm}$, $\Lambda_x \sim 430 \text{ nm}$, and $\Lambda_z \sim 550 \text{ nm}$. The surrounding silicon material has been removed to form a diagonal trench and isolated mesa structure to enable fiber taper probing.

A fiber-coupled swept wavelength (1565 - 1625 nm) laser source was used to measure the wavelength dependent forward transmission (\bar{T}) through the fiber taper, and a fiber splitter was used to monitor the signal in the backward propagating fiber taper mode (\bar{R}). With the taper aligned with the etched trench, the spectral and spatial properties of the PC cavity modes were probed directly (Fig. 3(a), taper position (ii)), as in Ref. [3]. The trench prevents the fiber taper from interacting with the unpatterned silicon, and light is coupled directly from the fiber taper into the high-Q PC cavity modes. Although this coupling is inefficient ($\Delta\bar{T} = 1\text{-}10\%$, $I \ll 1$), it

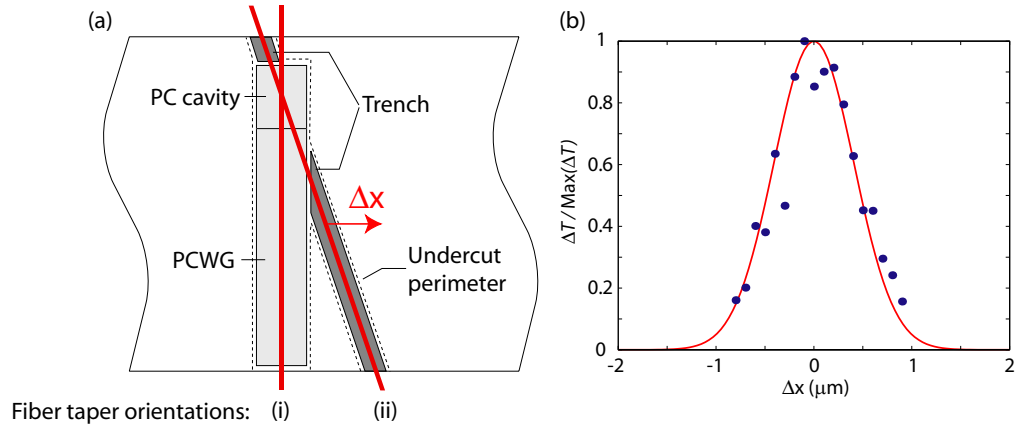


Fig. 3. (a) Illustration of the device and fiber taper orientation for (i) efficient PCWG mediated taper probing of the cavity, and (ii) direct taper probing of the cavity. (b) Normalized depth of the transmission resonance (ΔT) at $\lambda_o \sim 1589.7$, as a function of lateral taper displacement relative to the center of the PC cavity, during direct taper probing (taper in orientation (ii)).

allowed the frequency of the A_2^0 cavity mode to be independently determined.

In the device studied here, when the taper was aligned with the trench and positioned ~ 500 nm above the cavity, a sharp dip in \bar{T} was observed at a wavelength of $\lambda_o \sim 1589.7$ nm. It was confirmed that this was due to coupling to a localized cavity mode by studying the depth of the resonance as the taper was displaced laterally ($|\Delta x| > 0$) relative to the center of the PC-cavity. The measured normalized resonance depth as a function of taper displacement is shown in Fig. 3(b), and has a halfwidth of 480 nm, consistent with previous studies of the localized A_2^0 cavity mode [3].

The fiber taper was then aligned above and parallel to the PCWG (Fig. 3(a), taper position (i)). At taper-PCWG phase-matching wavelengths, \bar{T} decreases resonantly as power is coupled from the taper into the PCWG; coupling to the TE_1 PCWG mode was verified by studying the dispersive and spatial properties of the coupling, as in Ref. [42]. The fiber taper-PCWG coupling bandwidth was adjusted to overlap with the wavelength of the A_2^0 cavity mode using two mechanisms. Coarse tuning was obtained by adjusting, from sample to sample, the nominal hole size and longitudinal lattice constant (Λ_z) of the PCWG. Fine tuning of the coupler's center wavelength over a 100 nm wavelength range was obtained by adjusting the position, and hence diameter, of the fiber taper region coupled to the PCWG [42]. Different degrees of cavity loading were also studied by adjusting the number of periods (9-11) of air holes between the center of the PC cavity and the end of the PCWG. In the device studied below (shown in Fig. 2) the PC cavity was fabricated with 9 periods on the side adjacent the PCWG and 18 periods on the side opposite the PCWG.

Figure 4(a) shows the normalized reflected fiber signal, \bar{R} , for a taper diameter $d \sim 1 \mu\text{m}$, which aligns the taper-PCWG coupler bandwidth with the A_2^0 PC cavity mode wavelength. This signal is normalized to the taper transmission in absence of the PCWG, and since light passes through the taper-PCWG coupler twice, is given by $\bar{R} = \eta_{wg}^2 R_o$, where η_{wg} is the taper-PCWG coupling efficiency. Note that both R_o and η_{wg} are frequency dependent. In Fig. 4(a), the peak in \bar{R} around $\lambda \sim 1590$ nm corresponds to the phase-matched point of the fiber taper and the TE_1 PCWG mode. From the peak value of $\bar{R}_{\text{max}} = 0.53$, a maximum taper-PCWG coupling

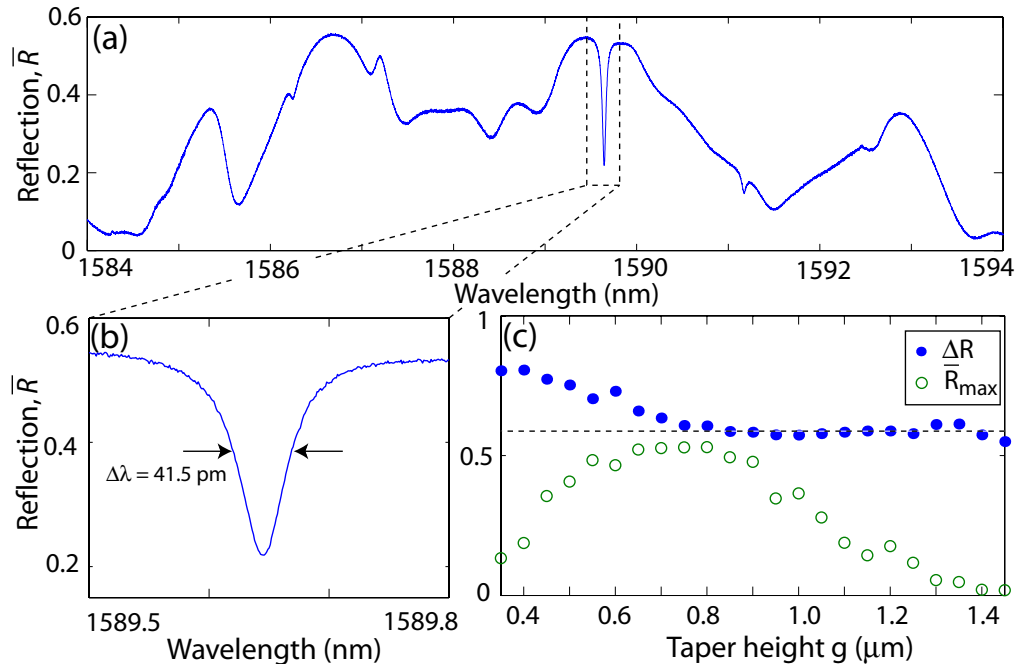


Fig. 4. (a) Measured reflected taper signal as a function of input wavelength (taper diameter $d \sim 1 \mu\text{m}$, taper height $g = 0.80 \mu\text{m}$). The sharp dip at $\lambda \sim 1589.7 \text{ nm}$, highlighted in panel (b), corresponds to coupling to the A_2^0 cavity mode. (c) Maximum reflected signal (slightly detuned from the A_2^0 resonance line), and resonance reflection contrast as a function of taper height. The dashed line at $\Delta R = 0.6$ shows the PCWG-cavity drop efficiency, which is independent of the fiber taper position for $g \geq 0.8 \mu\text{m}$.

efficiency of $\eta_{wg} \sim 73\%$ is estimated, where the off-resonant R_o is taken to be unity. This value is lower than the 97% obtained in previous work [21] due to coupling to additional higher-order (normal to the Si slab) PCWG modes which interfere with the coupling to the fundamental TE_1 PCWG mode for strong taper-PCWG coupling. This can be avoided in future devices by increasing the nominal PCWG hole size relative to that in the PC-cavity or reducing the Si slab thickness, effectively freezing out the higher-order PCWG modes [42].

The sharp dip in reflection at $\lambda \sim 1589.7 \text{ nm}$, shown in detail in Fig. 4(b), corresponds to resonant excitation of the A_2^0 PC cavity mode, as confirmed by the direct fiber probing of the cavity described above. The other broad features in \bar{R} correspond to weak Fabry-Pérot effects of the PCWG, and weak interference between the TE_1 mode and higher order PCWG modes. The reflected fiber taper signal as a function of taper-PCWG gap height, g , is shown in Fig. 4(c). For $g \geq 0.8 \mu\text{m}$, \bar{R}_{max} increases with decreasing g as the coupling from the fiber taper to the TE_1 PCWG mode becomes stronger. The reflection contrast, $\Delta R = 1 - R_o(\omega_o) = (\bar{R}_{\text{max}} - \bar{R}(\omega_o)) / \bar{R}_{\text{max}}$, remains constant, since the PCWG-cavity interaction is independent of the fiber taper to PCWG coupling. For smaller taper-PCWG gap heights, $g < 0.8 \mu\text{m}$, fiber taper coupling into higher order PCWG modes and radiation modes becomes appreciable, and \bar{R}_{max} decreases for decreased taper height. The corresponding increase in ΔR seen in Fig. 4(c) is a result of interference between the TE_1 mode and higher-order PCWG modes which are excited and collected by the taper, and is not a manifestation of improved coupling between the TE_1 PCWG mode and the A_2^0 PC cavity mode. Direct coupling between the taper and the cavity is

negligible here.

From a Lorentzian fit to the A_2^0 cavity resonance dip in $R_o(\omega)$, the normalized on-resonance reflected power is estimated to be $R_o(\omega_o) = 0.40$, corresponding to an undercoupled $K = 0.225$. The loaded quality factor as measured by the reflected signal linewidth is $Q_T = 3.8 \times 10^4$. Substituting these values into Eq. (4) gives the cavity mode quality factor due to parasitic loading and intrinsic losses, $Q_{i+P} = 4.7 \times 10^4$. Previous measurements of similar PC cavity devices without an external PCWG load yielded intrinsic quality factors of 4×10^4 [3], strongly indicating that the parasitic loading of the PC cavity by the PCWG is minimal, and $I \sim 1$ for this PC cavity-waveguide system. The high ideality of this coupling scheme should be contrasted with previous direct taper measurements of the PC cavities [3], whose coupling was limited to a maximum value $K = 0.018$, with an ideality of $I \sim 0.035$ (corresponding to a resonance depth of 7%, $Q_T = 2.2 \times 10^4$).

The efficiency of power transfer from the fiber taper into the PC cavity is given by $\eta_{in} = \eta_{wg} \Delta R \approx 44\%$. This corresponds to the *total* percentage of photons input to the fiber taper which are dropped by the PC cavity. Based upon these measurements, in the case of an internal cavity source such as an atom or a quantum dot, the efficiency of light collection into the fiber taper for this PC cavity system would be $\eta_{out} = \eta_{wg} \eta_0 \approx 13\%$ ($\eta_0 \approx 18\%$). As the tapers themselves are of comparably very low loss, with typical losses associated with the tapering process less than 10%, these values accurately estimate the *overall* optical fiber coupling efficiency. Finally, note that previous measurements of near-ideal coupling between the fiber taper and PCWG [21] indicate that by adjusting the PCWG as described above to improve η_{wg} , η_{in} and η_{out} can be increased to 58% and 18%, respectively. More substantially, adjustments in the coupling parameter K towards over-coupling by decreasing the number of air-hole periods between the PC cavity and the PCWG can result in significant increases in η_{in} and η_{out} with minimal penalty in loaded Q -factor for $I \sim 1$.

5. Nonlinear measurements

The nonlinear response of the PC cavity was studied by measuring the dependence of the reflected signal lineshape on the power input to the PCWG. Figure 5 shows wavelength scans of the cavity response R_o for varying power, P_i , input to the fiber taper. Each scan was obtained by dividing the normalized reflected signal, \bar{R} , by the slowly varying taper-PCWG coupler lineshape, $\eta_{wg}^2(\omega)$. In all of the measurements, the fiber taper was aligned near the optimal taper-PCWG coupling position, and the wavelength of the laser source was scanned in the direction of increasing λ . P_i was determined by taking taper insertion loss into account, and measuring the taper input power with a calibrated power meter.

Increasing the power in the fiber taper, and consequently the PCWG, results in three readily observable changes in R_o : (i) a decrease in the resonance contrast, ΔR_o , (ii) a shift $\Delta \omega_o$ in the resonance frequency ω_o , and (iii) broadening and asymmetric distortion of the resonance lineshape, eventually leading to a “snap” in the reflection response characteristic of bistability [43]. Here we use the theory presented in Section 3 to show that these features are due to nonlinear absorption and dispersion in the PC cavity.

Figure 6(a) shows P_d , the on-resonance power dropped into the PC cavity, as a function of P_i , the power incident on the cavity from the PCWG. P_d is measured from $P_d = \Delta R_o(P_i) P_i$, and P_i is related to the taper input power by $P_i = \eta_{wg}(\omega_o) P_t$. For small P_i , P_d increases with a constant slope equal to the “cold cavity” value of $\Delta R_o = 0.60$ measured in Section 4. For larger P_i , P_d becomes sub-linear versus P_i as loss due to nonlinear absorption becomes appreciable compared to the other loss channels of the PC cavity. In the context of the analysis of Section 3, γ^i increases with increasing P_d , degrading K , and decreasing ΔR_o (for $K < 1$). From the “cold cavity” η_0 and Q_T measured in the previous section, the power dependent $Q_{i+P}(P_i)$ can be

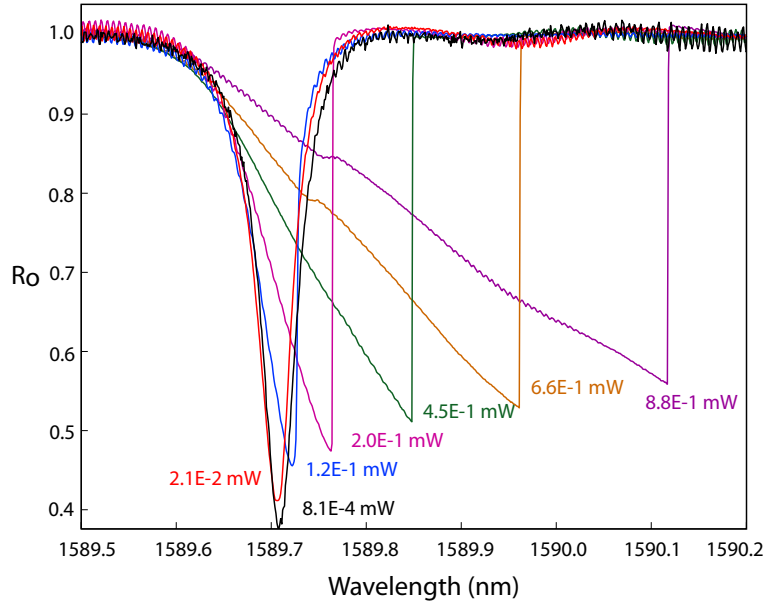


Fig. 5. (a) Measured cavity response as a function of input wavelength, for varying PCWG power (taper diameter $d \sim 1 \mu\text{m}$, taper height $g = 0.80 \mu\text{m}$).

extracted from $\Delta R_o(P_i)$ through the relation:

$$Q_{i+P}(P_i) = K(\Delta R_o(P_i)) \frac{Q_T(P_i = 0)}{\eta_0(P_i = 0)}. \quad (41)$$

Equation (41) is useful for powers where nonlinear effects distort the Lorentzian lineshape, and $\lambda_o/\delta\lambda$ is not an accurate measure of $Q_T(P_i)$. Using Eqs. (41) and (7), the internal cavity energy, U , can be calculated from P_i and ΔR_o .

Figure 6(b) shows a plot of the measured $\Delta\lambda_o$, the resonance wavelength shift, as a function of U [44]. This plot has several noteworthy properties. First, the wavelength shift is nonlinear in U , indicating that nonlinear processes such as free-carrier dispersion and heating through nonlinear absorption must be taking effect. Also, for small U the resonance wavelength is seen to blue shift. In the 1550 nm wavelength band of operation both dn_{Si}/dT and $n_{2,\text{Si}}$ are > 0 , while $d(\Delta n_{\text{FCD}})/dU < 0$, indicating that free-carrier dispersion is the dominant dispersive process at low input powers. For $U > 0.34 \text{ fJ}$ ($P_d > 10 \mu\text{W}$), the resonance wavelength begins to red shift, indicating that thermal or Kerr effects dominate for large internal cavity energy. Also, note that for a stored cavity energy as low as $U \sim 3 \text{ fJ}$ ($P_d \sim 100 \mu\text{W}$) the cavity response is bistable with $\Delta\lambda_o = 35 \text{ pm} \sim \sqrt{3}\delta\lambda/2$.

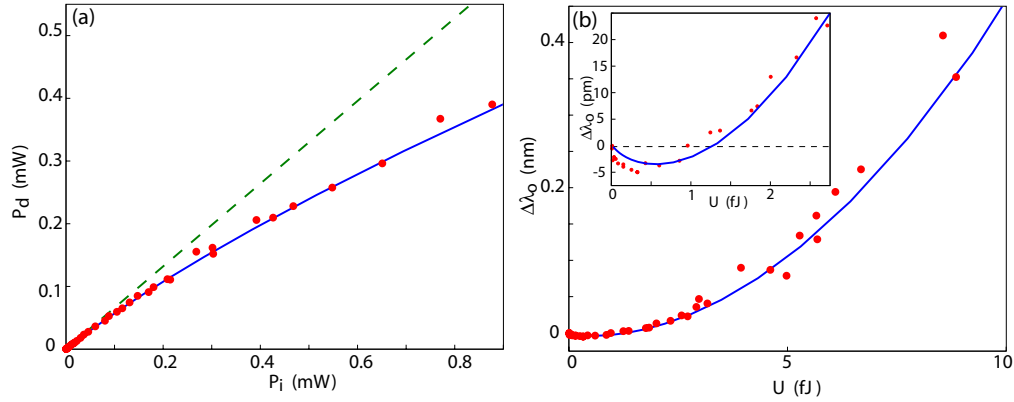


Fig. 6. (a) Power dropped (P_d) into the cavity as a function of power in the PCWG (P_i). The dashed line shows the expected result in absence of nonlinear cavity loss. (b) Resonance wavelength shift as a function of internal cavity energy. Solid blue lines in both Figs. show simulated results.

Table 1. Fixed parameters used in the model.

Parameter	Value	Units	Source
V_{TPA}	4.90	$(\lambda_o/n_{\text{Si}})^3$	FDTD ^b
V_{FCA}	3.56	$(\lambda_o/n_{\text{Si}})^3$	FDTD ^b
Γ_{TPA}	0.982	-	FDTD ^b
Γ_{FCA}	0.997	-	FDTD ^b
n_{Si}	3.45	-	[47, 34]
σ_{Si}	14.5×10^{-22}	m^2	[47, 34]
ζ_{Si}^e	8.8×10^{-28}	m^3	[47, 34]
ζ_{Si}^h	4.6×10^{-28}	m^3	[47, 34]
$n_{2,\text{Si}}$	4.4×10^{-18}	$\text{m}^2 \cdot \text{W}^{-1}$	[28]
β_{Si}	8.4×10^{-12}	$\text{m} \cdot \text{W}^{-1}$	[28] ^a
dn_{Si}/dT	1.86×10^{-4}	K^{-1}	[48]

^a Average of the two quoted values for Si(110) and Si(111).

^b Calculated from FDTD generated fields of the A_2^0 cavity mode of the graded square lattice cavity studied here.

In order to estimate the contributions of the various nonlinear processes to the effects discussed above, the absorptive, $P_d(P_i)$, and dispersive, $\Delta\lambda(P_i)$, data were fit using the model presented in Section 3. Specifically, Eqs. (9-11) were solved for P_d and U as a function of P_i , and Eq. (25) was used to calculate $\Delta\lambda_o$. The free parameters in this model were taken as: (i) the effective free-carrier lifetime, τ , (ii) the effective thermal resistance of the PC cavity, $\Gamma_{\text{th}}dT/dP_{\text{abs}}$, and (iii) the fraction of the “cold cavity” loss which is due to linear absorption (as

opposed to radiation), $\eta_{\text{lin}} = \gamma_{\text{lin}}/(\gamma_{\text{lin}} + \gamma_{\text{rad}})$. The material and modal constants used are listed in Table 1.

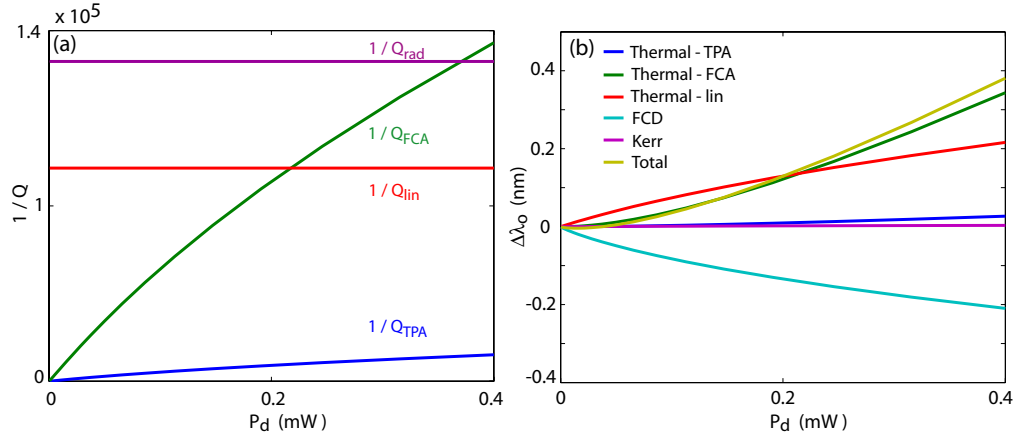


Fig. 7. (a) Simulated effective quality factors for the different PC cavity loss channels as a function of power dropped into the cavity. (b) Contributions from the modeled dispersive processes to the PC cavity resonance wavelength shift as a function of power dropped into the cavity. (Simulation parameters: $\eta_{\text{lin}} \sim 0.40$, $\Gamma_{\text{th}}dT/dP_{\text{abs}} = 27$ K/mW, $\tau^{-1} \sim 0.0067 + (1.4 \times 10^{-7})N^{0.94}$ where N has units of cm^{-3} and τ has units of ns.)

As has been observed in studies of silicon optical waveguides [29], we find that a strong dependence of τ on carrier density is required for our model to accurately reproduce *both* the dispersive and absorptive data represented in Figs. 7(a) and (b). In order to account for a carrier density dependent lifetime in our model the following procedure was used. With $\Gamma_{\text{th}}dT/dP_{\text{abs}}$ and η_{lin} held fixed, $\tau(P_i)$ was determined for each input power from a least squares fit to $\Delta\lambda_o(P_i)$ and $P_d(P_i)$. Since there are two data points for each input power, one dispersive and one absorptive, the optimum $\tau(P_i)$ has a non-zero residual error. This procedure was repeated for a range of values for $\Gamma_{\text{th}}dT/dP_{\text{abs}}$ and η_{lin} . For a fixed value of η_{lin} , the fits were robust in $\Gamma_{\text{th}}dT/dP_{\text{abs}}$ with the sum of the least square residual of $\tau(P_i)$ clearly minimized for an optimal value of $\Gamma_{\text{th}}dT/dP_{\text{abs}}$. This procedure, however, was only found to constrain $\eta_{\text{lin}} > 0.15$. Within this range of η_{lin} the quality of the fits does not change significantly, with the optimal functional form of τ changing slightly and the optimal value of $\Gamma_{\text{th}}dT/dP_{\text{abs}}$ varying between $\sim 15 - 35$ K/mW. Based on estimates of η_{lin} from studies of loss in silicon microdisk resonators fabricated using the same SOI wafers and the same processing techniques [45], and by comparing the etched surface area seen by the PC cavity mode to that seen by a microdisk mode, we chose to use $\eta_{\text{lin}} \sim 0.40$ for the PC cavity. With this value of η_{lin} the optimal value of the effective cavity thermal resistance, $\Gamma_{\text{th}}dT/dP_{\text{abs}}$, was found to be 27 K/mW, of the same order of magnitude as the result calculated in Ref. [46] for a similar membrane structure. Finally, the point-by-point least-squared optimum values of $\tau(P_i)$ were then fit as a function of the effective free-carrier density N , using a curve of the form $\tau^{-1} = A + BN^\alpha$. Using this $\tau(N)$, smooth fits to measured $P_d(P_i)$ and $\Delta\lambda(P_i)$ were obtained, shown as solid blue lines in Fig. 6.

The various components of the total cavity loss rate and resonance shift based upon the above fits to the measured data are shown in Fig. 7. It can be seen that although TPA does not dominate the PC cavity response, the free-carriers it generates and the resulting free carrier dispersion and absorption drive the nonlinear behavior of the silicon PC cavity at low and high input powers, respectively. The fit effective free-carrier lifetime, shown in Fig. 8, shows

similar characteristics to that obtained by Liang et al. [29], demonstrating a significant fall-off in τ for large N , but with a smaller saturated lifetime. Both the pronounced decay in τ and the low ~ 0.5 ns value of the high-carrier density free-carrier lifetime are significantly different from that found in bulk Si, and are most likely related to carrier diffusion and surface effects owing to the extremely large surface-to-volume ratio of the PC cavity, the small length scales involved (~ 200 nm feature size), and the small size scale of the optical mode [40]. This small effective free-carrier lifetime is consistent with other recent experimental results of highly porous silicon optical structures [31, 36, 41]. It should, however, be noted that the bulk Si TPA coefficient was used in modelling the nonlinear response of the PC cavity, which given the above comments may not be accurate due to surface modification of TPA. As the effects of free-carrier lifetime and two-photon absorption on the behaviour of the dispersive and absorptive nonlinear response of the PC cavity are somewhat intertwined, further studies will be necessary to concretely separate these two phenomena in porous Si structures such as the photonic crystals of this work.

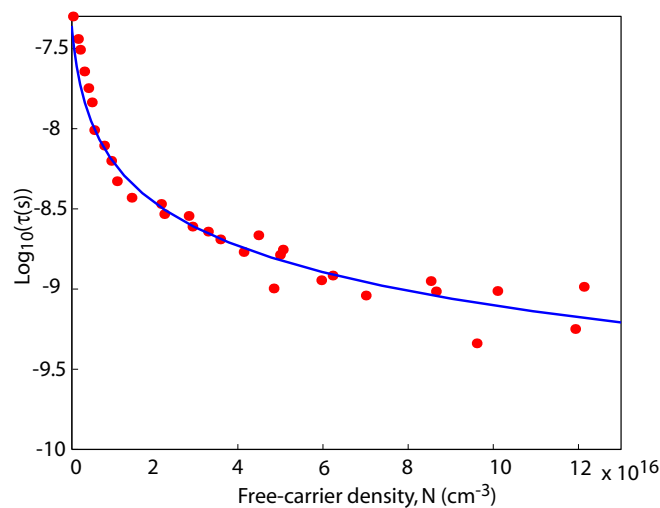


Fig. 8. Dependence of free-carrier lifetime on free-carrier density (red dots) as found by fitting $\Delta\lambda_o(P_i)$ and $P_d(P_i)$ with the constant material and modal parameter values of Table 1, and for effective PC cavity thermal resistance of $\Gamma_{th}dT/dP_{abs} = 27$ K/mW and linear absorption fraction $\eta_{lin} = 0.40$. The solid blue line corresponds to a smooth curve fit to the point-by-point least-squared fit data given by $\tau^{-1} \sim 0.0067 + (1.4 \times 10^{-7})N^{0.94}$, where N is in units of cm^{-3} and τ is in ns.

6. Summary

In conclusion, we have demonstrated an optical fiber coupling scheme to efficiently source and collect light from high-Q ultra-small mode volume PC cavities. By employing a PCWG which supports a mode which is simultaneously spatially mode matched with the high-Q PC cavity mode of interest and phase matched with an optical fiber taper, efficient fiber-PCWG-cavity coupling is enabled. A total fiber-to-cavity coupling efficiency of 44% is demonstrated, which for the case of an internal cavity emitter corresponds to a radiated photon collection efficiency of 13%. These values are not fundamental limits of this technique, and can be improved through fine tuning of the photonic crystal. The efficiency of this fiber coupling method was then ex-

ploited to probe the steady-state nonlinear optical properties of the PC cavity. The effect of two-photon absorption, free-carrier absorption and dispersion, Kerr self-phase modulation, and thermo-optic dispersion, on the response of the PC cavity was considered. Optical bistability at fiber input powers of $250 \mu\text{W}$ was observed, and a free-carrier lifetime with high carrier density value as low as $\sim 0.5 \text{ ns}$ is inferred from nonlinear absorptive and dispersive measurements of the PC cavity. Along with applications to nonlinear optics, this optical fiber evanescent coupling based approach should be useful for future experiments in integrated micro-optics with photonic crystals, and in particular to cQED systems employing photonic crystals, where quantum computing and communication protocols demand high optical fidelity.

Acknowledgments

The authors thank Matthew Borselli for helpful discussion. This work was supported by the Charles Lee Powell foundation. KS would also like to thank the Hertz foundation for its support through a graduate fellowship.